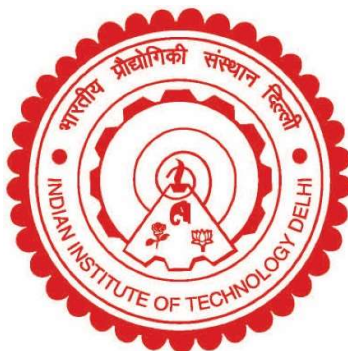


**MICROFABRICATION AND PERFORMANCE
EVALUATION OF MICROFLUIDIC MEMBRANELESS
ENERGY CONVERSION DEVICES FOR HYDROGEN
GENERATION AND UTILIZATION**

BISWAJIT SAMIR DE



**DEPARTMENT OF CHEMICAL ENGINEERING
INDIAN INSTITUTE OF TECHNOLOGY DELHI
DECEMBER 2022**

© Indian Institute of Technology Delhi (IITD), New Delhi, 2022

**MICROFABRICATION AND PERFORMANCE
EVALUATION OF MICROFLUIDIC MEMBRANELESS
ENERGY CONVERSION DEVICES FOR HYDROGEN
GENERATION AND UTILIZATION**

by

BISWAJIT SAMIR DE

Department of Chemical Engineering

Submitted

In fulfilment of the requirements for the degree of

DOCTOR OF PHILOSOPHY

to the



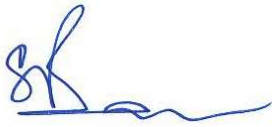
INDIAN INSTITUTE OF TECHNOLOGY DELHI

DECEMBER 2022

Dedicated to my late grandmother Smt. Urmila De

Certificate

This is to certify that the thesis entitled “**Microfabrication and Performance Evaluation of Microfluidic Membraneless Energy Conversion Devices for Hydrogen Generation and Utilization**” submitted by **Mr. Biswajit Samir De** to the Indian Institute of Technology Delhi, for the award of the degree of Doctor of Philosophy, is a record of the original bonafide research work carried out by him. He has worked under my supervision and has fulfilled the requirements, which to my knowledge, has reached the requisite standard for the submission of this thesis. The results contained in this thesis have not been submitted in part or full to any University or Institute for the award of any degree or diploma.



Prof. Suddhasatwa Basu
Supervisor
Department of Chemical Engineering
Indian Institute of Technology Delhi



Prof. Neeraj Khare
Co-supervisor
Department of Physics
Indian Institute of Technology Delhi

Acknowledgments

‘What we know is a drop, what we do not know is an ocean’ – Sir Isaac Newton.

My journey so far, to explore the possibility of not knowing and the pursuit for knowledge was possible because Prof Suddhasatwa Basu accepted me as his prospective Ph.D. student. I will remain forever indebted for Prof Basu’s contribution in my evolution as a researcher. My co-supervisor, Prof Neeraj Khare, has nourished me with his streamlined guidance and helped me overcome the challenges in every step of my research. I convey my deepest gratitude to Prof Anastasia Elias for providing me the opportunity to visit her group at the University of Alberta and helping me with her timely guidance.

I am thankful to my thesis committee members, Prof Anupam Shukla, Prof Ali Haider, and Prof Praveen Ingole, for finding time to discuss despite their tight schedule. I am thankful to the administrative and technical staff of the Department of Chemical Engineering and the Nanoscale Research Facility (NRF) for providing me with the facilities and tool to perform research.

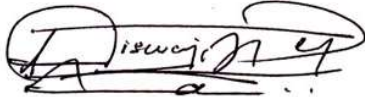
I am grateful to the Science and Engineering Research Board (SERB) to provide financial support to visit the University of Alberta and the Ministry of Electronics and Information Technology (MeitY) India for supporting my research at IIT Delhi.

The journey will be incomplete without the support my companions Dr. Aditya Singh, Ram Ji Dixit, and Vicky Dhongde. I am grateful to Dr. Harikrishnan and Vigness for being supportive when I was walking on thin ice. A shoutout to my friends Shantanu Banerjee, Saroj Samantaray, Debarghya Saha, Jeetendra Nanda, Ramdayal Panda, Vivek Dalvi and Rajat Dhawan for their help, motivation, and moral support.

I convey my heartfelt gratitude to my late grandmother, Urmila De, for her prayers and blessings. I extend my deepest love and respect to my parents Samir Kumar De and Manimala

De, and brother Prasenjit De, whom I admire. Finally, my journey so far would not have been possible without the prayer, support, and sacrifices of my sweet loving wife, Priyanka Arya De.

I pray and thank the Almighty, for showing the light and guide me away from the darkness.

A handwritten signature in black ink, appearing to read "Biswajit De". The signature is stylized with loops and is written over a horizontal line.

Biswajit Samir De

Abstract

The typical electrolysis cell/ fuel cell components like membrane-electrode assembly (MEA), gas/liquid diffusion layer, and flow plates were eliminated by the strategic implementation of microfluidics. Microfluidic devices rendered membraneless operation owing to the prevalence of plane parallel flow in the microchannel. Hydrogen (H_2) production by water splitting in a membraneless microfluidic electrolysis cell (μ EC) allows flexibility in the choice of pH. An applied voltage induced a two-phase flow of gas products and liquid electrolyte in the μ EC microchannel. The gas products intermixing in the microchannel were averted by optimizing the electrolyte flow rate, which balanced the inertial and viscous forces acting on a fluid.

The development of the μ EC is limited by the complexity in fabrication the low hydrogen throughput, and gas purity in membraneless operation. The present research sheds light on the investigation and development of the μ EC that encompasses techniques to improve the reaction kinetics, ease the manufacturability, and enhance mass transfer in the microfluidic electrolysis cell to increase the hydrogen production rate with negligible gas crossover.

An asymmetric electrolyte configuration (acidic catholyte and alkaline anolyte) was used in the μ EC to drastically reduce the overpotential of water electrolysis by utilizing the electrochemical neutralization energy. The μ EC operating at 10 mA cm^{-2} current density could electrolyze water at 1.58 V for the asymmetric electrolyte which was less as compared to that in acidic and alkaline electrolyte. The μ EC advancement was limited by the availability of a bifunctional catalyst compatible with microfabrication techniques. The scalable synthesis of a nickel nitride/ nickel (Ni_3N/Ni) bifunctional catalyst was demonstrated. Ni microelectrodes were microfabricated, and nitridation and N-H grafting of the electrodes was achieved by ammonia plasma. The μ EC with Ni_3N/Ni exhibited a current density of $263.73 \text{ mA cm}^{-2}$ at 2.5 V, a stable 6 h operation, and a performance efficiency of 99.86%. The multiple fabrication

steps and low H₂ production rate impedes the scale-up of the μ EC for commercial application. The fabrication of the μ EC was elucidated, and the H₂ production increased by implementing a 3D-printed μ EC with flow-through porous electrodes. The μ EC attained an H₂ production rate of 15 mL min⁻¹ with a current density of 748 mA cm⁻² at 2.5 V. Accelerated stress testing was performed for 370 h with a fluctuating current density as a stressor. Minimum degradation of the electrodes was observed with a slight decrease in the performance of the μ EC. Negligible gas crossover at the optimized flow rate was observed in the μ ECs, which was analyzed by gas chromatography. The optimized flow rate of operation was obtained whereby, no gas intermixing takes place, by equating drag force acting on the gas bubble and opposing interfacial tension force at the triple phase boundary of electrode – gas bubble – liquid electrolyte interfaces in the direction of the flow.

The H₂ produced in the μ EC was consumed in a microfluidic fuel cell (μ FC) operating in tandem to generate micropower. In tandem operation, asymmetric electrolyte configuration could not be used due to opposite nature of operation of electrolysis cell and fuel cell. However, the results of the acidic and alkaline electrolyte were compared for the μ EC and tandem μ EC- μ FC operation. A voltage applied to the μ EC induces two-phase flow in the μ EC- μ FC, resulting in the evolution of H₂ and O₂ gases that are transported to the μ FC by convection, and consumed to generate power. The μ EC- μ FC delivered 14.68 mW cm⁻² maximum power density with μ EC operating at 99.98% energy conversion efficiency and the μ FC attaining up to 50% fuel utilization with 4 h of stable tandem operation.

The outcome of the thesis paves the way for future research towards the scale-up of the μ EC for integration with renewable energy systems for on-site off-grid green hydrogen production.

सार

विशिष्ट इलेक्ट्रोलिसिस सेल/फ्यूल सेल के पुरजे जैसे की मेम्ब्रेन-इलेक्ट्रोड असेंबली (MEA), गैस/लिक्विड डिफ्यूजन लेयर और फ्लो प्लेट्स को माइक्रोफ्लुइडिक्स के समरिक्त क्रियांवयन के द्वारा समाप्त कर दिया गया था। माइक्रोचैनल में प्रचंड विस्कोस फोर्स की व्यपक्ता के कारण माइक्रोफ्लुइडिक अपकर्णों को मेम्ब्रेनलेस बना दिया गया था। एक मेम्ब्रेनलेस माइक्रोफ्लुइडिक इलेक्ट्रोलिसिस सेल (μEC) में वाटर स्प्लिटिंग से हाइड्रोजन उत्पादन के पीएच चुनाव में स्वाधीनता की अनुमति देता है। माइक्रोचैनल में स्थापित इलेक्ट्रोड्स पर वोल्टेज लगाने पर उसमे गैस उत्पाद और लिक्विड इलेक्ट्रोलाइट के टू-फेज फ्लो का गठन होता है। माइक्रोचैनल मी इंटरमिक्सिंग होन वाले गैस प्रोडक्ट्स को इलेक्ट्रोलाइट फ्लो रेट को अनुकूलित करके ताल दिया गया, जो एक फ्लूइड पर कार्य करने वाले इन्टियल और विस्कोस फोर्सेस को संतुलित करता है। एक असममित इलेक्ट्रोलाइट कॉन्फिगरेशन (अम्लीय कैथोडिक और क्षारीय एनोडिक) का उपयोग μEC में किया गया था ताकी इलेक्ट्रोकेमिकल न्यूट्रलाइजेशन एनर्जी का उपयोग करके वाटर इलेक्ट्रोलिसिस की ओवरपोटेंशियल को कम किया जा सके | 10 mA cm^{-2} करंट डेंसिटी पर काम करने वाला μEC एसिमेट्रिक इलेक्ट्रोलाइट में 1.58 V पर पानी को इलेक्ट्रोलाइज किया था, जो की एसिडिक और क्षारीय इलेक्ट्रोलाइट की तुलना में कम था। माइक्रोफैब्रिकेशन तकनीक के साथ संगत एक द्वि-कार्यात्मक उत्प्रेरक की उत्थान के करन μEC की उन्नति सीमित थी। निकेल नाइट्राइड/निकेल ($\text{Ni}_3\text{N}/\text{Ni}$) द्वि-कार्यात्मक उत्प्रेरक के स्केलेबल

संश्लेषण का प्रदर्शन किया गया। नी माइक्रोइलेक्ट्रोड्स को माइक्रोफैब्रिकेट किया गया था, और नाइट्रिडेशन और इलेक्ट्रोड के एनएच ग्राफिटिंग को अमोनिया प्लाज़्मा द्वारा प्राप्त किया गया था। Ni₃N/Ni के साथ μ EC ने 2.5 V पर 263.73 mA cm⁻² का करंट डेंसिटी मिला, एक स्थिर 6 घंटे का ऑपरेशन , और 99.86% की प्रदर्शन दक्षता प्रदर्शित की। लिथोग्राफी के द्वारा विभिन्न फेब्रिकेशन स्टेप्स और कम एच₂ उत्पादन दरव्यवसायिक उनुप्रयोग के लिए μ EC के स्केल अप को बाधित करती है । 3D प्रिंटिंग के जरिए μ EC के निर्माण को आसान किया गया और प्रवाह के मध्यम से पोरस इलेक्ट्रोड के साथ μ EC को बनाकर H₂ प्रोडक्शन में वृद्धि हुई। μ EC ने 2.5 V पर 748 mA सेमी⁻² के वर्तमान घनत्व के साथ 15 एमएल मिनट⁻¹ की एच₂ उत्पादन दर प्राप्त किया। एक तनाव के रूप में उतार चढ़ाव वाले वर्तमान घनत्व के साथ 370 घंटे के लिए त्वरित तनाव परीक्षण किया गया था। μ EC के कार्य में मामूली कमी के साथ इलेक्ट्रोड का न्युनातम गिरावट देखा गया। अनुकूलित प्रवाह दर पर कोई भी गैस क्रॉसओवर माइक्रोईईसी में नहीं देखा गया, जिस्का विश्लेषण गैस क्रोमैटोग्राफी द्वारा किया गया था। ऑपरेशन की अनुकूलित प्रवाह दर प्राप्त की गई थी, जिससे कोई गैस इंटरमिक्सिंग नहीं होती है, गैस बुलबुले पर अभिनय करने वाले ड्रैग फोर्स की बराबरी करके और इलेक्ट्रोड की ट्रिपल-फेज सीमा पर इंटरफेसियल टेंशन फोर्स का विरोध करते हुए - गैस बबल - लिक्विड इलेक्ट्रोलाइट इंटरफेस की दिशा में बहे।

μ EC में उत्पादित H₂ की खपत एक माइक्रोफ्लुइडिक ईंधन सेल (μ FC) में की गई जो माइक्रोपावर उत्पादन करने के लिए मिलकर काम कर रही थी | अग्रानुक्रम संचालन में, इलेक्ट्रोलाइज़र और ईंधन

सेल के संचालन की विपरीत प्रकृति के कारण असममित इलेक्ट्रोलाइट कॉन्फिगरेशन का उपयोग नहीं किया जा सकता है। हालांकि, अम्लीय और क्षारीय इलेक्ट्रोलाइट के परिणामों की तुलना μEC और अग्रानुक्रम $\mu\text{EC}-\mu\text{FC}$ ऑपरेशन के लिए की गई थी। μEC पर लागू एक वोल्टेज $\mu\text{EC}-\mu\text{FC}$ में दो टू-फेज फ्लो को प्रेरित करता है, जिसके परिणाम स्वरूप H_2 और O_2 गैसों का विकास होता है जिन्हें कंवेक्टिव फ्लो द्वारा μFC में ले जाया जाता है और पावर जनरेशन करने के लिए उपभोग होता है। $\mu\text{EC}-\mu\text{FC}$ में μEC की 99.88% ऊर्जा रूपांतरण दक्षता पर संचालन के साथ 14.68 मेगावाट सेमी-2 अधिकतम बिजली घनत्व दिया और μFC ने 4 घंटे के स्थिर संचालन के साथ 50% ईंधन उपयोग दक्षता प्राप्त किया।

Table of Contents

Title	Page No.
Certificate	i
Acknowledgements	ii
Abstract	iv
सर	vi
Table of contents	ix
List of figures	xii
List of tables	xviii
Chapter 1: Introduction	1-18
1.1 Natural Gas based H ₂ Production	2
1.2 Coal Gasification based H ₂ Production	5
1.3 Renewable Energy based H ₂ Production	6
1.4 Microfluidic Energy Conversion	8
1.4.1. Microfluidic Electrolysis Cell	12
1.4.2. Microfluidic Fuel Cell	15
1.5 Thesis Objectives	16
1.6 Thesis Organization	17
Chapter 2: Literature Review	19-35
2.1 Energy Conversion in Electrochemical Cells	19
2.2 Microfluidic Electrolysis Cell	21
2.3 Microfabrication of the Microfluidic Electrochemical Cell	24
2.4 Microchannel Shape and Electrode Position	28
2.5 Electrolytes	30
2.6 Catalysts	31
2.7 Microfluidic Electrolysis Cell Performance	31
2.8 Research Gaps and Scope of Thesis	34
Chapter 3: Experimental Methods	37-53
3.1 Microfluidic Device Fabrication	37
3.1.1 Lithography-based Microfabrication	37

3.1.2 Additive Manufacturing	39
3.1.3 Thin Film-based Catalyst Fabrication	42
3.2 Physico-chemical Characterization	43
3.2.1 X-ray powder diffraction	43
3.2.2 Scanning Electron Microscopy (SEM) and Energy Dispersive X-ray spectroscopy.	43
3.2.3 X-ray Photoelectron Spectroscopy (XPS)	44
3.3 Electrochemical Analysis	44
3.4 Microfluidic Device Performance Evaluation with Visual Inspection	45
3.4.1 Asymmetric Electrolyte Configuration Microfluidic Electrolysis Cell	46
3.4.2 Alkaline Microfluidic Electrolysis Cell	49
3.4.3 Additively Manufactured Microfluidic Electrolysis Cell	50
3.4.4 Microfluidic Electrolyzer – Fuel Cell Tandem Operation	53
Chapter 4: Electrochemical Neutralization Energy-Assisted Water Electrolysis in Membraneless Microfluidic Electrolysis Cell.	54-73
4.1 Results and Discussions	54
4.1.1 Electrochemical Neutralization	54
4.1.2 Electrochemical Characterizations	59
4.1.3 Efficiency Calculations	70
4.2 Conclusions	72
Chapter 5: Microfabrication of Ammonia Plasma-Assisted Nickel Nitride-Nickel Thin-Film Electrodes for Overall Water Splitting in a Membraneless Microfluidic Electrolysis Cell.	74-95
5.1 Results and Discussions	74
5.1.1 Physical Analysis	74
5.1.2 Electrochemical Analysis	82
5.1.3 μ EC Performance Evaluation	87
5.2 Conclusions	94
Chapter 6: Performance Evaluation and Accelerated Stress Testing of Additively Manufactured Membraneless Microfluidic Electrolysis Cell	96-110
6.1 Results and Discussions	96
6.1.1 Performance Evaluation of μ EC	98
6.1.2 Accelerated Stress Testing	106

6.2 Conclusions	110
Chapter 7: Hydrogen Generation and Utilization in a Two-phase Flow Membraneless Microfluidic Electrolysis Cell - Fuel Cell Tandem Operation for Micropower Application	111-130
7.1 Results and Discussion	111
7.1.1 Efficient transport of H^+ (acidic electrolyte) or OH^- (alkaline electrolyte) ions across the microelectrodes of the μEC and μFC	112
7.1.2 Efficient generation of separated H_2 and O_2 streams in the μEC and transport to μFC	114
7.1.3 Ensure that the μEC and μFC are physically connected and electrically disconnected.	117
7.1.4 Performance evaluation of μEC - μFC	118
7.1.5 Efficiency calculation for the μEC - μFC tandem operation	123
7.2 Conclusions	129
Chapter 8: Conclusions and Future Prospective	131-135
8.1 Conclusions	132
8.2 Future Prospective	134
Appendix	136-150
References	151-176
Resume of Author	177-179

List of Figures

Figure No.	Title	Page No.
Figure 1.1	Different colour codes of H ₂ based on the production routes.	2
Figure 1.2	The benefits of microfluidics in the electrolysis cell system can be realized by downsizing the characteristic dimension leading to an upsizing of the intrinsic fluid properties and rightsizing the electrolysis cell's electrochemical performance.	8
Figure 1.3	The strategic implementation of microfluidics eliminates the number of components of a typical electrolysis cell (left) and condenses the electrolysis cell to a single chip, performing electrochemical energy conversion on fingertips.	14
Figure 2.1	Schematic representation of the electrochemical cells with components.	20
Figure 2.2	The stacked, multilayer structure of a typical state-of-art electrolysis cell can be implemented on a single chip using microfluidics.	23
Figure 2.3	Schematic representation of various microchannel shapes and the relative position of the electrodes with respect to the channel. (a) T-shaped microchannel, (b) Y-shaped microchannel, (c) converging flow microchannel, (d) straight microchannel with baffle, and (e) straight microchannel with baffle and mesh electrodes.	27
Figure 3.1	Steps for the fabrication of the microfluidic electrolysis cell, A: Channel fabrication, B: Electrode fabrication, and C: Alignment and bonding.	38
Figure 3.2	Microfluidic electrolysis cell (a) schematic representation of the 3D-printed parts, and (b) assembled 3D-printed parts.	40
Figure 3.3	Alkaline microfluidic electrolysis cell experimental setup for visual and electrochemical analysis.	46
Figure 3.4	The schematic representation of the μ EC with dimensions. Inset 1 explains the mechanism of electrochemical	48

	neutralization occurring at the electrodes and liquid junction potential at the interface of the two electrolytes at different pH. Inset 2 depicts the separation of gas products evolving at the electrode surface by a viscous flow induced Segre'-Silberberg effect.	
Figure 3.5	Microfluidic electrolysis cell's schematic representation of the 3D-printed parts, and assembled 3D-printed parts.	50
Figure 3.6	Experimental setup for the performance evaluation and accelerated stress testing of the microfluidic electrolysis cell.	51
Figure 3.7	Schematic representation of proof-of-concept with dimensions for the membraneless μ EC- μ FC tandem operation in acidic and alkaline electrolyte.	53
Figure 4.1	pH dependence of electrolyte on cell potential from the Nernst equation. The red line represents HER at the cathode, and the blue line depicts OER at the anode.	57
Figure 4.2	The schematic representation of membraneless microfluidic electrolysis cell with dimensions. Inset 1 explains the mechanism of electrochemical neutralization occurring at the electrodes and liquid junction potential at the interface of the two electrolytes at different pH. Inset 2 depicts the separation of gas products evolving at the electrode surface by a viscous flow induced Segre'-Silberberg effect.	58
Figure 4.3	Membraneless μ EC (a) current-voltage response curve, and (b) electrochemical impedance spectroscopy assessed under asymmetric, acid, and alkaline electrolytes at 1.4 mL min^{-1} flow rate.	60
Figure 4.4	Schematic 2D representation of an infinitesimal longitudinal cross-sectional element of the microchannel demonstrating Segre'-Silberberg effect for a laminar viscous flow.	65
Figure 4.5	The Y-junction at exit is used to separate gas products from the device operating at a constant applied potential of 1.8V with a	66

	varying flow rate of asymmetric electrolyte at (a) 0.8 mL min ⁻¹ (b) 1 mL min ⁻¹ (c) 1.2 mL min ⁻¹ , and (d) 1.4 mL min ⁻¹ .	
Figure 4.6	Polarization curve as a function of flow rate (0.8 – 1.4 mL min ⁻¹) for asymmetric electrolyte configuration for water electrolysis.	67
Figure 4.7	The stability in operation of membraneless μ EC electrolysis cell is evaluated by performing (a) chronoamperometry at a constant applied potential of 1.8 V for 4 h, and (b) the collected H ₂ was analyzed by GC to check gas crossover.	69
Figure 5.1	(a) XRD spectra of Ni, NN15:350, NN30:350, NN45:350, NN15:400, NN15:450, NN15:350N ₂ , FE-SEM images of (b) bare Ni, (c) NN15:350, and (d) NN15:350 cross-sectional view.	76
Figure 5.2	EDX mapping of NN15:350 showing the distribution of (a) Ni (b) N and (c) composite image of Ni and N and (d) EDX spectrum.	77
Figure 5.3	Core-level high-resolution XPS spectra of NN15:350, NN30:350, NN45:350, NN15:400, NN15:450, and NN15:350N ₂ in (a) Ni2p region (b) O1s, and (c) N1s region. (d) XPS depth profile for NN15:350 showing the change in Ni, O and N elemental composition as a function of depth up to 30 nm and relative XPS spectra in (e) Ni2p (f) N1s (g) O1s region.	79
Figure 5.4	(a) LSV curves for HER and OER, PEIS for (b) HER, and (c) OER activity of Pt, Ni, and NN15:350, CV at different scan rates in the non-faradaic region for (d) NN15:350, and (e) Ni, (f) CA for NN15:350 at voltages corresponding to 10 mA cm ⁻² .	83
Figure 5.5	(a) Current-voltage response, and (b) PEIS at 1.2 mL min ⁻¹ for Pt and NN15:350 for the μ EC.	88
Figure 5.6	(a) Schematic representation of the μ EC, (b) Qualitative visual inspection of gas product separation with a varying flow rate in the μ EC at an intermediate position and at the exit.	89
Figure 5.7	Effect of electrolyte flow rates on (a) current-voltage response, inset depicts the current density response in the applied voltage	92

	range 2.25 – 2.5 V (b) PEIS for the μ EC with NN15:350 catalyst. Stability analysis of the μ EC with NN15:350 electrodes evaluated by (c) chronoamperometry, and (d) gas chromatogram for product purity determination.	
Figure 6.1	(a) Schematic representation of the additively manufactured μ EC with porous electrodes, electrochemical performance evaluation (b) linear sweep voltammetry (LSV) at various electrolyte velocity (0.34 – 0.16 m s ⁻¹), galvanostatic impedance spectroscopy (GEIS) concerning the varying electrolyte velocity (0.34 – 0.16 m s ⁻¹) at (c) 68 mA cm ⁻² , (d) 172 mA cm ⁻² , and (e) 518 mA cm ⁻² .	97
Figure 6.2	(a) Equivalent circuit diagram used for the impedance spectra. Ohmic resistance (R_{Ω}), charge transfer resistance (R_{ct}), and mass transfer resistance (R_{mt}) concerning the electrolyte velocity (0.16 – 0.34 m s ⁻¹) in the μ EC at (b) 68 mA cm ⁻² , (c) 172 mA cm ⁻² , and (d) 518 mA cm ⁻² .	102
Figure 6.3	(a) Percentage (%) crossover of H ₂ concerning the varying electrolyte velocity (0.16 – 0.34 m s ⁻¹), gas chromatogram for the qualitative identification of gas crossover at (b) 0.34 m s ⁻¹ , (c) 0.28 m s ⁻¹ , (d) 0.23 m s ⁻¹ , and (e) 0.16 m s ⁻¹ , (f) chronoamperometry at 2.5 V and 0.34 m s ⁻¹ electrolyte velocity.	104
Figure 6.4	Electrochemical characterization of the accelerated stress testing (AST) (a) chronopotentiometry with an applied dynamic stressor, comparison of the performance of the μ EC before and after AST by (b) linear sweep voltammetry (LSV), and (c) galvanostatic electrochemical impedance spectroscopy (GEIS).	107
Figure 6.5	SEM images of the electrode (a) before AST, (b) cathode after AST, (c) anode after AST, (d) XRD spectra of the electrodes before AST and, cathode and anode after AST, and XPS spectra of (e) Ni 2p, (f) Pt 4f, and (g) O 1s for the electrodes before AST, cathode after AST, and anode after AST.	109

Figure 7.1	Schematic representation of proof-of-concept with dimensions for the membraneless μ EC- μ FC tandem operation in acidic and alkaline electrolyte. The inset depicts the electrical barrier between μ EC and μ FC and the transport of fuel and oxidant generated at μ EC to μ FC for utilization to generate micropower.	113
Figure 7.2	Still images of the bubble formation and trajectory in the μ EC- μ FC microchannel at different locations (columns) with varying flow rates (rows) ($< 1.2 - 1.8 \text{ mL min}^{-1}$)	115
Figure 7.3	Effect of electrolyte flow rate on the performance of the membraneless two-phase flow μ EC- μ FC: (a) polarization and (b) power density curves in the acidic electrolyte; (c) polarization and (d) power density curves in alkaline electrolyte.	120
Figure 7.4	Effect of the μ EC operating voltages on the μ FC performance: (a) polarization, and (b) power density curves in the acidic electrolyte; (c) polarization, and (d) power density curves in alkaline electrolyte.	121
Figure 7.5	Chronoamperometry to test the resilience of the membraneless two-phase flow μ EC- μ FC tandem operation.	122
Figure 8.1	Schematic representation of the Solar – μ EC module for green H_2 production.	135
Figure A1	The 2D geometries of the double-Y shaped channel and double-T shaped channel used in the COMSOL Multiphysics modelling.	144
Figure A2	Velocity profile and concentration profile obtained at the end of 1000 s for the double-T shaped and double Y-shaped channels.	145
Figure A3	XRD spectra of Pt thin film showing preferentially oriented (111) plane of the face-centered cubic structure (ICDD # 00-004-082).	145

Figure A4	(a) relative XRD peak intensities of Ni (111) peak and (b) calculated crystallite size from Ni (111) peak using Scherrer equation.	146
Figure A5	(a) Enlarged view of 2- NN15:350, 3- NN30:350 (111) peak showing large FWHM for 3- NN30:350 (b) Lorentzian peak fit to show the FWHM.	146
Figure A6	(a) FE-SEM image and (b) EDX spectrum of the Pt:100 thin film.	146
Figure A7	XPS elemental survey scan of NN15:350 (black), NN30:350 (blue), NN45:350 (magenta), NN15:400 (green), NN15:450 (red), NN15:350N ₂ (violet).	147
Figure A8	XPS depth profile of NN15:350 sample (a) O1s spectra in etching time of 0 s to 120 s (step size 30 s) showing diminishing -OH and C=O peaks of adventitious oxygens (b) N1s spectra in etching time of 0 s to 120 s (step size 30 s) showing diminishing Ni-O and N-H peaks.	147
Figure A9	Comparison of HER activity of sputtered Pt with NN15:350 and Pt plate.	148
Figure A10	Tafel plots for the (a) HER and (b) OER activity of NN15:350, Ni, and Pt catalyst	148
Figure A11	Current density as a function of scan rates for the estimation of double-layer capacitance C_{dl} .	148
Figure A12	XRD spectra of the NN15:350 depicting the effect of OER on the catalyst.	148
Figure A13	Schematic representation of the dynamic current stressor imposed on the μEC for accelerated stress testing (AST).	150

List of Tables

Table No.	Title	Page No.
Table 1.1	Brief description of the various routes of H ₂ production.	3
Table 4.1a	Typical state – of – art electrolysis cell with components and system cost	62
Table 4.1b	Asymmetric μ EC with components and system cost	62
Table 5.1	Comparison of HER activity of NN15:350 catalyst with other non-noble electrocatalyst in alkaline electrolyte	84
Table 5.2	Comparison of OER activity of NN15:350 catalyst with other non-noble electrocatalyst in alkaline electrolyte	84
Table 6.1	Comparison of the performance of various μ EC	100
Table 7.1	Efficiency for the μ EC- μ FC tandem operation for various μ FC operating voltages	125
Table 7.2	A few works of literature on μ FCs for comparison of ε_{fuel}	127
Table 7.3	Performance of the μ FC concerning the choice of the fuel and oxidant.	128
Table A1	Values of the dimensionless number estimated for flow characterization in microchannel for asymmetric electrolyte configuration in microfluidic electrolysis cell.	142
Table A2	Dimensionless number for flow characterization in microchannel in the microfluidic membraneless alkaline microfluidic electrolysis cell.	143
Table A3	Dimensionless number for flow characterization in microchannel in the additively manufactured microfluidic membraneless electrolysis cell.	143
Table A4	Dimensionless number for flow characterization in the microfluidic electrolysis cell – fuel cell tandem device.	143
Table A5	μ FC operating voltage and their corresponding current density and current	144